Contents lists available at ScienceDirect

Heliyon

journal homepage: www.cell.com/heliyon

Research article

Engineering nanostructured Ag doped α-MnO₂ electrocatalyst for highly efficient rechargeable zinc-air batteries

Ababay Ketema Worku [a], Delele Worku Ayele [a,b,*], Nigus Gabbiye Habtu [a,c,**], Mehary Dagnew Ambaw [d]

[a] Bahir Dar Energy Center, Bahir Dar Institute of Technology, Bahir Dar University, Bahir Dar, P. O. Box 26, Ethiopia
[b] Department of Chemistry, College of Science, Bahir Dar University, P. O. Box 79, Bahir Dar, Ethiopia
[c] Faculty of Chemical Engineering, Bahir Dar Institute of Technology, Bahir Dar University, Bahir Dar, P. O. Box 26, Bahir Dar, Ethiopia
[d] Department of Industrial Chemistry, College of Science, Bahir Dar University, P. O. Box 79, Bahir Dar, Ethiopia

HIGHLIGHTS

- Ag doped α-MnO₂ electrode for rechargeable zinc–air battery was prepared via a facile co-precipitation technique.
- Ag doped α-MnO₂ electrode shows lower charge transfer resistance associated to un-doped MnO₂ electrode.
- Ag doped α-MnO₂ shows enhanced ORR kinetics in oxygen electrode potential.
- The capacitance performance of Ag doped α-MnO₂ electrodes was highly improved.
- Ag doped α-MnO₂ electrode showed energy density of 69.3 W h kg−1 and power density of 722.9 W kg−1.

ARTICLE INFO

ABSTRACT

Engineering of highly active, and non-precious electrocatalysts are vital to enhance the air-electrodes of rechargeable zinc-air batteries (ZABs). We report a facile co-precipitation technique to develop Ag doped α-MnO₂ nanoparticles (NPs) and investigate their application as cathode materials for ZABs. The electrochemical and physical characteristics of α-MnO₂ and Ag doped α-MnO₂ NPs were compared and examined via CP, CV, TGA/DTA, FT-IR, EIS, and XRD analysis. CV result displayed higher potential and current for ORR in Ag doped α-MnO₂ NPs than α-MnO₂; but, ORR performance decreased when the Ag doping was raised from 7.5 to10 mmol. Moreover, α-MnO₂ and Ag doped α-MnO₂ NPs showed 2.1 and 3.8 electron transfer pathway, respectively, showing Ag doped α-MnO₂ performance to act as an active ORR electrocatalyst for ZABs. The EIS investigation exhibited that charge-transfer resistance for Ag doped α-MnO₂ was extremely lower associated to the MnO₂ demonstrating that the successful loading of Ag in α-MnO₂. A homemade ZAB based on Ag–MnO₂-7.5 showed a high open circuit potential, low ohmic resistances, and excellent discharge profile at a constant current density of 1 mA/g. Moreover, Ag–MnO₂-7.5 show a specific capacity of 795 mA h g⁻¹ with corresponding high energy density ~875 Wh kg⁻¹ at 1 mA cm⁻² discharging conditions.

1. Introduction

The development of sustainable and renewable energy storage technologies to satisfy future needs has become increasingly critical in order to deal with the growing consumption of fossil fuels due to increased environmental pollution challenges [1, 2, 3]. Energy has attracted much attention as the basic driving force of economic development, and chemical power sources such as supercapacitors, lithium-ion batteries, fuel cells and metal air batteries have made great progress [4, 5, 6]. Among different energy storage devices, zinc-air batteries (ZABs) are supposed to be one of the promising power sources for next-generation applications in electric vehicles, grid storage,

and portable electronic devices [7, 8]. The recent development in the rechargeable alkaline ZABs has gained better attention because of its environment-friendly, low cost, large-scale grid storage capacity, safety and high energy density [9, 10]. Oxygen evolution reaction (OER) and oxygen reduction reaction (ORR) performance are the main challenges in the preparation and commercialization of rechargeable ZABs [11, 12]. Efforts in enhancing the performance of electrocatalysts for OER and ORR are limited by the poor air electrodes or bi-functional electrocatalysts, due to the short-lived cycles and sluggish kinetics [13]. Recently, various catalysts with excellent OER and ORR performance have been investigated for ZABs. ORR regulates the discharge process of the battery, and OER regulates the charge process of the battery [14, 15]. The standard catalysts for OER and ORR are Ir/Ru and Pt-based electrocatalysts, respectively [16, 17]. Their utilization is restricted by limited bi-functional catalytic activity, weak stability, and high cost [10]. Thus, non-noble metal oxides such as MnO_2, Co_3O_4, and CuO are emerging as alternative catalysts to precious metal-based materials for rechargeable ZABs [18, 19]. From non-noble metal oxides, manganese dioxide is studied as the most potential electrocatalyst for rechargeable ZABs due to its environmental friendliness, low cost, considerable catalytic activity, abundance, and low toxicity [13, 20]. However, MnO_2 nanomaterials suffer from low electronic conductivity and limited catalytic performance. The stoichiometric ratio, morphologies, particle size, and crystallographic structures affect the catalytic activity of MnO_2 nanoparticles [21, 22]. Hence, among the phases of MnO_2 nanoparticles α-MnO_2 shows the best catalytic activity as reported from previous works [23]. Different strategies such as preparing nanocomposites, doping with metal ions, tuning morphology, have been designed to improve intrinsic activity, catalytic activity and of MnO_2 nanoparticles [24, 25]. Hence, doping MnO_2 nanoparticles with cations such as Fe, Ag and Ni is an efficient technique to enhance its catalytic activity and electronic characteristics [26, 27]. Reports show that Ag-based nanoparticles are a potential candidate for zinc-air battery cathode materials due to their low overpotential [13]. Moreover, the addition of Ag changes the structure and particle size of α-MnO_2 which is advantages to provide more active sites [10]. Here, a simple co-precipitation approach is developed for synthesizing Ag doped α-MnO_2 nanoparticles (NPs). This method have the following key advantages such as an energy-saving approach, low cost, simple, and low preparation temperature. In this research, Ag doped α-MnO_2 catalysts were developed using a simple co-precipitation approach. Additionally, this work aims to investigate at how Ag ion doping in MnO_2 affects the nanomaterials' crystalline structure, shape, particle size, and catalytic activity as well as how they are used in ZABs.

2. Experimental sections

2.1. Materials

All reagents are purchased with analytical grade and utilized without any additional purification. Potassium permanganate (99% $KMnO_4$ Sisco), sodium hydrogen carbonate ($NaHCO_3$ 98% Sigma Aldrich), aqueous ammonia (NH_4OH, 35%), manganese sulphate ($MnSO_4 \cdot H_2O$, 99%) and silver nitrate (98% $AgNO_3$) from Sigma Aldrich. Distilled water (DW) is utilized as a solvent throughout the experimental work.

2.2. Synthesis

Ag doped MnO_2 and MnO_2 NPs were synthesized by a simple co-precipitation approach. Initially, 30 mmol $MnSO_4 \cdot H_2O$ and preferred mole of (2.5, 5, 7.5, 10, and 15 mmol) $AgNO_3$ were dissolved in 100 mL DW and 20 mmol $KMnO_4$ was dissolved in 100 mL DW. The solution was heated to 80 °C. While stirring $NaHCO_3$ solution (1 M) was added dropwise until the solution reached to a pH of 9. The solution was stirred at 300 rpm with a temperature of 80 °C for about 3 h. The solution was washed with DW several times, filtered and dried at 110 °C for 12 h. Finally, the obtained product was calcined at 400 °C for 4 h. A similar method was implemented for the preparation of MnO_2 NPs. The only modification was that the absence of $AgNO_3$ into the $KMnO_4$ and $MnSO_4 \cdot H_2O$ solution. The samples were labelled as Ag–MnO_2-2.5, Ag–MnO_2-5, Ag–MnO_2-7.5, Ag–MnO_2-10 and Ag–MnO_2-15 based on the doping level of $AgNO_3$ (2.5, 5, 7.5, 10 and 15 mmol), respectively. Figure 1 shows the detailed illustration of Ag doped MnO_2 NPs prepared through co-precipitation technique.

2.3. Characterization

X-ray diffraction (XRD) was used to examine the crystalline structures and the phases of synthesized materials using Cu Kα radiation working at 30 mA and 40 kV in the range of 10–80°. FTIR was carried out to investigate the functional groups. The thermal properties of the as-prepared materials were examined by TGA/DTA. The electrochemical behaviours were analyzed by electrochemical impedance spectroscopy (EIS), chronopotentiometry (CP) and cyclic voltammetry (CV).

2.4. Electrochemical measurement

To determine the electrochemical activity of as-prepared catalysts a three electrode cell configuration at 0.1 M KOH aqueous electrolyte were
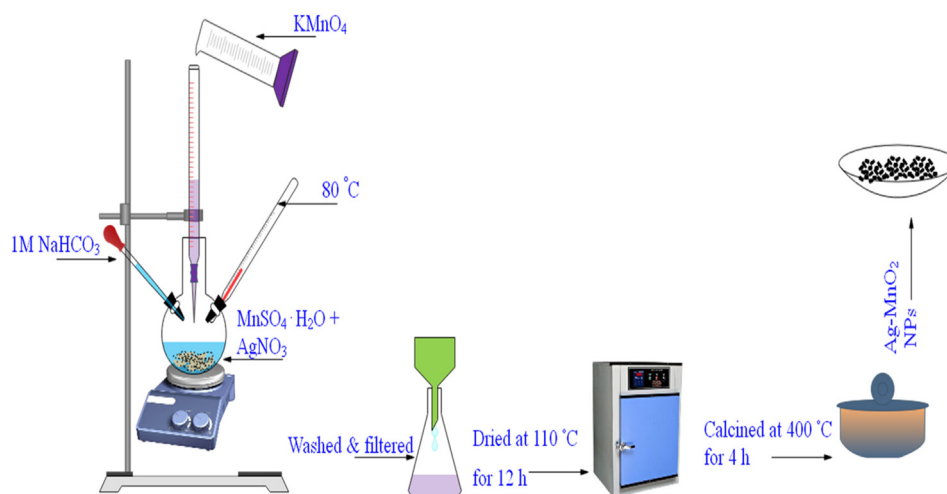

Figure 1. Diagram of the experimental setup for α-MnO_2 and Ag doped α-MnO_2 NPs preparation via Co precipitation approach.

performed using an electrochemical workstation of CHI760E. Platinum coil, glassy carbon and Ag/AgCl were utilized as counter, working and reference electrodes, correspondingly. The working electrode was prepared by casting MnO_2 and Ag doped MnO_2 solution on a glassy carbon substrate. The sample suspension was prepared by mixing 3.5 mg of MnO_2 and Ag doped MnO_2 nanomaterials with 3.5 mg of carbon powder (to increase electronic conductivity) in isopropanol-water solution (2.5 mL) with 7:3, volume/volume ratio. The sample ink was mixed ultrasonically for 10 min and then 15 µL of this solution was pipetted onto the working electrode. The electrolyte saturation via oxygen was done for 30 min in the electrochemical examination process.CV was studied at various scan rates (5, 10, 20, 50, and 100 mV s^{-1}) in the potential window range of +0.1 to -0.7 V (vs Ag/AgCl). CV results were utilized to estimate the specific capacitance (C_s) of each electrode according to Eq. (1) [28].

$$C(F/g) = \frac{A}{\Delta V \times v \times m} \qquad (1)$$

where ΔV, A, m and v are sweep potential window, integral area of the CV loop, mass of the electrode materials and scan rate, respectively. The power density (P in W/kg) and energy density (E in W h/kg) of the as prepared electrode can be calculated using CV profile at various scan rates using Eqs. (2) and (3) [29]:

$$E = \frac{C\Delta V^2}{2} \qquad (2)$$

$$P = \frac{E}{t} \qquad (3)$$

where ΔV, t and C are potential window during the CV measurements process (V), discharge time of the CV curves (s), and specific capacitance (F/g), respectively. The EIS were examined in the frequency interval of 0.01 kHz–100 kHz at 5 mV amplitude. CP was used to study the discharge property of the as-prepared electrode at 1 A g^{-1} current density.

2.5. Zinc-air battery assembly and performance testing

Zinc-air battery test were performed through a home-made fabricated zinc-air cell device. In the ZAB test polished zinc plate, carbon paper coated with as-prepared nanoparticles and 6 M KOH were used as anode, the air cathodes and electrolyte, correspondingly. The air electrodes were developed using as-synthesized catalysts mixing with conductive graphite powder and grinded using agate mortar for 15 min. Then, 15

wt.% PVDF was added to the above mixture and stirred for 12 h. The mixture was coated with a catalyst loading of 2.6 mg cm^{-2} on carbon paper (gas diffusion layer) and dried at 85 °C for 1 h. Resistance, open-circuit potentials and CP of ZABs were record using a CHI600E electrochemical workstation to obtain the impedance, open-circuit profiles and discharge performance, respectively.

3. Results and discussion

3.1. Structural properties

The crystalline nature and phase purity of α-MnO_2 and Ag loaded MnO_2 NPs were studied using XRD at 0.02°/s scan rate in a 2θ range of 10°–80°. Figure 2 shows the diffraction pattern of α-MnO_2 and different concentrations (2.5, 5, 7.5, 10, and 15 mmol) of silver doped α-MnO_2 nanoparticles. All as-synthesized samples showed diffraction peaks at 2-theta 12.67°, 17.99°, 25.67° 28.62°, 37.58°, 41.86°, 49.66°, 56.12°, 60.16°, 65.26°, 69.48°, 72.86° corresponding to the (1 1 0), (2 0 0), (2 2 0), (3 1 0), (4 0 0), (3 0 1), (4 1 1), (6 0 0), (5 2 1), (0 0 2), (5 4 1) and (3 1 2) crystalline planes, respectively. Hence, all the diffraction peaks are matched with space group 14/m 87 and the standard values of tetragonal α-MnO_2 (JCPDS 44-0141) [30, 31]. It can be observed that after Ag loading no peak of Ag or Ag_2O contents were detected due to very small amount of dopant. However, small rise in peak intensity of silver doped α-MnO_2 NPs has been identified because of the radius of the Mn ion is smaller than the radius of the Ag ion [29, 32]. The slight increase in peak intensity and the lack of diffraction of impurities indicate that Ag atoms have been effectively loaded into the lattice of α-MnO_2 NPs. Average crystallite size of as synthesized α-MnO_2 and Ag loaded MnO_2 NPs were calculated via Scherer method (Eq. 4).

$$D = \frac{K\lambda}{\beta \cos\theta} \qquad (4)$$

where λ, D, θ, K and β were wavelength, average crystallite size, scattering angle, shape factor with value of 0.9, and full width half maximum, respectively. The average crystallite size of α-MnO_2, Ag–MnO_2-2.5, Ag–MnO_2-5, Ag–MnO_2-7.5, Ag–MnO_2-10 and Ag–MnO_2-15 were 3.49, 4.39, 4.57, 4.79, 4.85 and 4.93 nm, respectively. Silver doping increase crystallite size of the as papered NPs because of silver addition into tunnels.

3.2. Morphological analysis

SEM analysis of the morphology of the as-prepared α-MnO_2 and Ag–MnO_2-7.5 NPs is shown in Figure 3. The catalyst α-MnO_2 SEM micrographs revealed well-defined, nanoscale cuboidal-shaped particles. As a result of the doping impact of the Ag NPs, Ag–MnO_2-7.5 revealed smooth cuboidal shaped nanoparticles. Additionally, in good accord with the XRD observation, the average diameters of the nanoparticles of α-MnO_2 Ag–MnO_2-7.5 are 18 nm and 23 nm, respectively. As seen in Figure 3a and b, the doping of Ag results in the smoothing of the morphology of the as-prepared nanomaterial in addition to increasing the particle size of α-MnO_2.

3.3. The elemental analyses via ICP-OES

Atomic compositions ICP-OES analyses of the as-prepared samples were performed to confirm the Mn and Ag loading in the Ag-doped MnO_2 NPs. The as-prepared nanoparticle was dissolved in a concentrated acidic solution (HCl:HNO3, 3:1 v/v by volume) to conduct the ICP-OES analysis. The Ag and Mn concentrations in the Ag-doped MnO_2 NPs are shown in Table 1. Additionally, for Ag–MnO_2 (0.025 M), Ag–MnO_2 (0.05 M), Ag–MnO_2 (0.075 M), Ag–MnO_2 (0.1 M), and Ag–MnO_2 (0.125 M) nanoparticles, the Ag/Mn doped molar ratio was 0.025, 0.066, 0.086, 0.137, and 0.103, respectively. ICP-OES analysis results revealed that
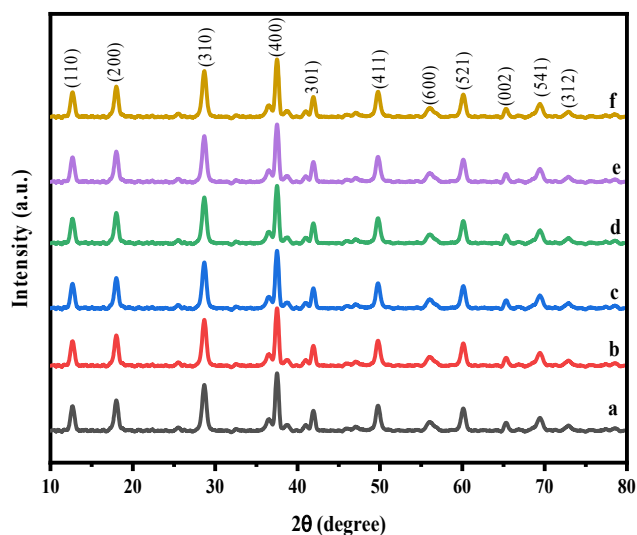

Figure 2. XRD profile of; (a) pure α-MnO_2, (b) Ag–MnO_2-2.5, (c) Ag–MnO_2-5, (d) Ag–MnO_2-7.5, (e) Ag–MnO_2-10 and (f) Ag–MnO_2-15 NPs.
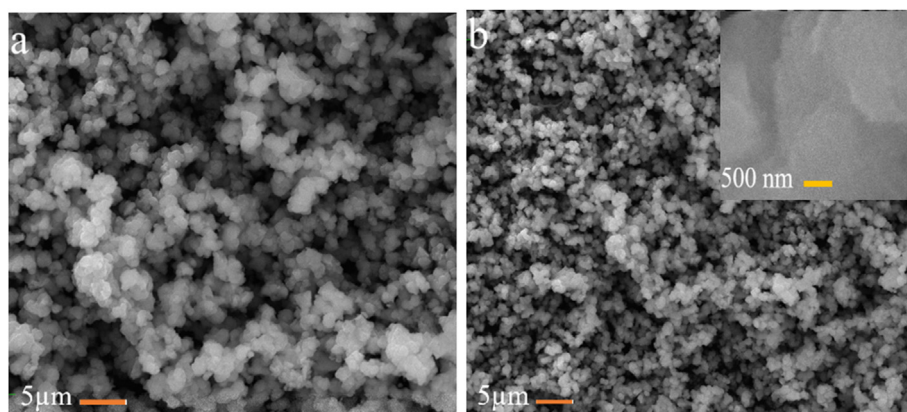
Figure 3. SEM images of a) α-MnO$_2$ and b) Ag doped α-MnO$_2$ NPs.

Table 1. Results of the ICP-OES investigation of Ag-doped MnO$_2$ nanoparticles.

Nanomaterials	Ag (mmol/L)	Mn (mmol/L)	Ag/Mn
Ag–MnO$_2$-2.5	0.013	0.504	0.026
Ag–MnO$_2$-5	0.027	0.473	0.057
Ag–MnO$_2$-7.5	0.033	0.451	0.073
Ag–MnO$_2$-10	0.039	0.439	0.088
Ag–MnO$_2$-15	0.047	0.421	0.11
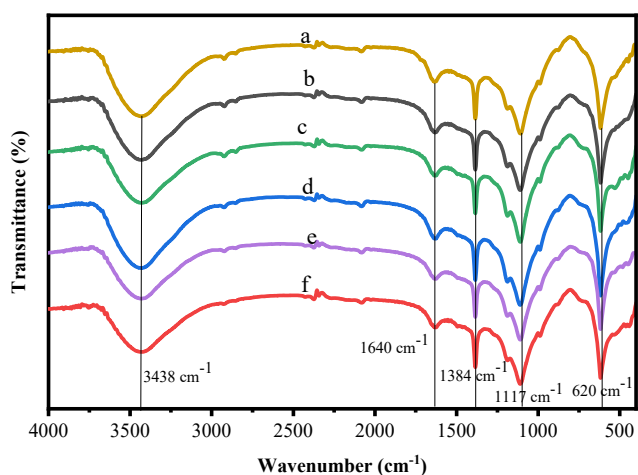
Figure 4. FTIR bands of; (a) pure α-MnO$_2$, (b) Ag–MnO$_2$-2.5, (c) Ag–MnO$_2$-5, (d) Ag–MnO$_2$-7.5, (e) Ag–MnO$_2$-10 and (f) Ag–MnO$_2$-15 NPs.

0.125 M and 0.1 M Ag–MnO$_2$ nanoparticles had larger Ag/Mn molar ratios than the others, which had an impact on their thermal, structural, and electrochemical properties.

3.4. Functional group analysis

FTIR spectra of α-MnO$_2$ and Ag loaded MnO$_2$ NPs were conducted in the range of 4000–400 cm^{-1} to identify the existence of functional groups and displayed in Figure 4. The absorption peak detected around 3438 cm^{-1} corresponding to the hydroxyl group and might be consigned to the stretching vibration of O–H bond, which was originated on the surface of the MnO$_2$ nanoparticles via water adsorption. The absorption peak at 1640 cm^{-1} and 1384 cm^{-1} corresponding to the bending vibration of O–H group [33]. The existence of more water adsorbed in Ag loaded MnO$_2$ NPs show that the tunnel of Ag-doped MnO$_2$ slightly accumulated water. The band at 1117 cm^{-1} may be ascribed to the

Mn–O–Mn stretching vibration, which describes the MnO$_6$ octahedral formation [34]. Moreover, the peaks at 522 cm^{-1} shows the Mn–O stretching vibration [35, 36].

3.5. TGA/DTA analysis

The thermal properties of the α-MnO$_2$ and Ag loaded MnO$_2$ NPs have been studied using thermogravimetric-differential thermal analysis (TGA/DTA) starting from room temperature to 900 °C at a heating rate of 10 °C/min in air atmosphere as shown in Figure 5. The TGA/DTA analysis of α-MnO$_2$ and Ag loaded MnO$_2$ NPs are shown in Figure 5(a and b). In the decomposition process of α-MnO$_2$ three stages weight loss were observed. The first 0.26 mg mass loss detected below 126 °C is associated to the dehydration of crystal water. The endothermic peak of DTA result observed at 64.8 °C corresponding with water bands adsorbed on the surface of the as-prepared material (Figure 5(b)). Moreover, the next 0.28 mg weight loss can be allied to the phase alteration of MnO$_2$ to Mn$_2$O$_3$. The corresponding endothermic peak of DTA curve is presented at 535.9 °C. The last 0.61 mg weight loss observed between 446–683 °C consistent to the phase conversion of Mn$_2$O$_3$ to Mn$_3$O$_4$ [37]. The resultant exothermic peak of DAT profile is detected around 689 °C. Similarly, in the decomposition process of Ag loaded MnO$_2$ NPs three stages weight loss were observed. The first 0.277 mg mass loss detected below 115 °C is associated to the dehydration of crystal water. The endothermic peak of DTA result observed at 69.75 °C corresponding with water bands adsorbed on the surface of the as-prepared material (Figure 5 (b)). Moreover, the next 0.283 mg weight loss can be allied to the phase alteration of MnO$_2$ to Mn$_2$O$_3$. The corresponding endothermic peak of DTA curve is presented at 533.2 °C. The last 0.42 mg weight loss observed between 470 °C–879 °C consistent to the phase conversion of Mn$_2$O$_3$ to Mn$_3$O$_4$. The resultant exothermic peak of DAT profile is detected around 687 °C. Hence, based on the TGA data investigation, the weight loss of α-MnO$_2$ and Ag doped MnO$_2$ NPs were 16.28% and 14%, respectively.

3.6. Electrochemical behavior analysis

3.6.1. CV behavior study

CV was conducted to study the electrochemical properties of α-MnO$_2$ and Ag loaded MnO$_2$ NPs at various doping level applying the potential in the range of −0.7 V–0.1 V vs Ag/AgCl electrode. Figure 6a displays O$_2$-saturated and unsaturated CV pattern of bare GCE, α-MnO$_2$/GCE and Ag loaded MnO$_2$/GCE electrodes in the presence of 0.1 M KOH solution at different scan rate. Figure 6b shows the CV behaviors of O$_2$-saturated and unsaturated bare GCE at a scan rate of 20 and 50 mV/s with 0.1 M KOH solution. It is detected that the reduction peak potential of oxygen purged bare GCE appeared at −0.325 V and −0.34 V with the reduction peak current of 10.37 μA and 23.2 μA at a scan rate of 20 and 50 mV/s,
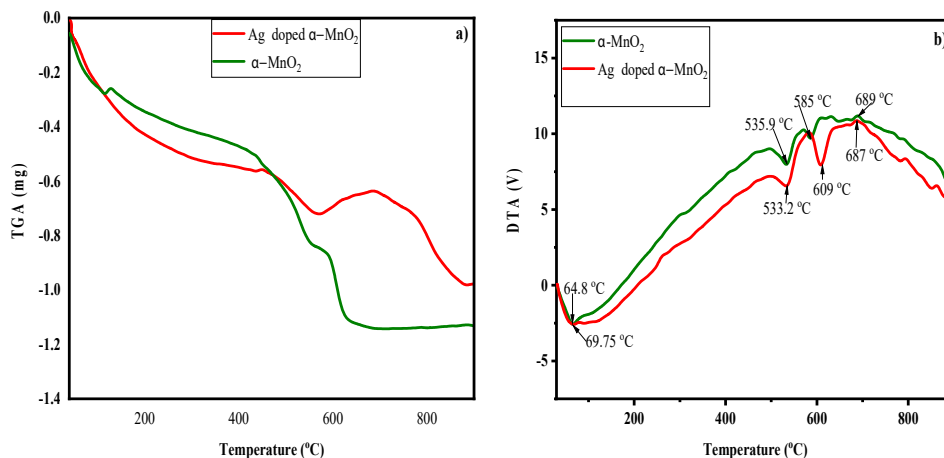
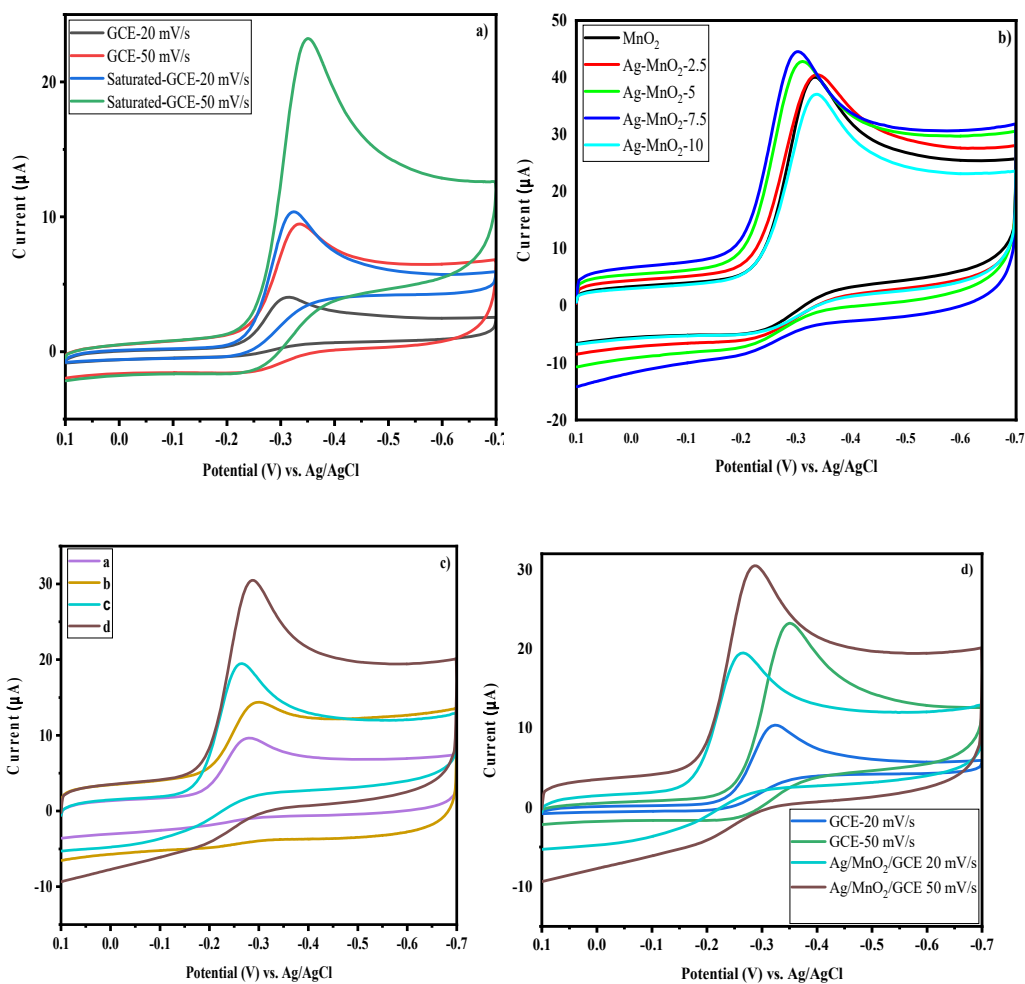**Figure 5.** (a) TGA curve of α-MnO$_2$ and Ag–MnO$_2$ NPs, (b) DTA profile of α-MnO$_2$ and Ag–MnO$_2$ NPs.

Figure 6. CV pattern of (a) GCE unsaturated and saturated in O$_2$-saturated at 20 and 50 mV/s, (b) MnO$_2$, Ag–MnO$_2$-2.5, Ag–MnO$_2$-5, Ag–MnO$_2$-7.5, and Ag–MnO$_2$-10 modified electrodes saturated in O$_2$-saturated at 100 mV/s, (c) Saturated and unsaturated Ag–MnO$_2$-7.5 modified electrode (a; unsaturated Ag–MnO$_2$/GCE at 20 mV/s, b; unsaturated Ag–MnO$_2$/GCE at 20 mV/s, c; saturated Ag–MnO$_2$/GCE at 20 mV/s and d; saturated Ag–MnO$_2$/GCE at 50 mV/s) (d) Saturated Ag–MnO$_2$-7.5/GCE and bar GCE electrodes with 0.1 M KOH solution.

respectively. Compared with the absence of oxygen, the reduction peak current of bare GCE is smallest, which are 4.03, and 9.4 at a scan rate of 20 and 50 mV/s, respectively. Figure 6c displays the CV pattern MnO$_2$, Ag–MnO$_2$-2.5, Ag–MnO$_2$-5, Ag–MnO$_2$-7.5, and Ag–MnO$_2$-10 modified electrodes saturated with O$_2$ at a scan rate of 100 mV/s. The reduction potential value of as-prepared nanoparticles are in the order of −0.29 V > −0.306 V > −0.33 V > −0.34 V > −0.35 V for Ag–MnO$_2$-7.5 > Ag–MnO$_2$-5 >Ag–MnO$_2$-2.5 > MnO$_2$ > Ag–MnO$_2$-10, respectively.

Among the as-prepared samples of Ag doped MnO$_2$, 7.5 mmol of Ag doped MnO$_2$ presented highest ORR potential and current (−0.29 V, 44.5 µA) compared to MnO$_2$ (−0.33 V, 40 µA) and 10 mmol (−0.33 V, 37 µA) of MnO$_2$. This evidence clearly indicated that the optimum doping of Ag onto MnO$_2$ is 7.5 mmol. Moreover, compared with O$_2$ saturated and unsaturated Ag–MnO$_2$-7.5 modified electrode, the peak current of Ag/MnO$_2$/GCE was increased dramatically after O$_2$ saturatation and the peak potential shifted to the more positive value (Figure 6c) [38].
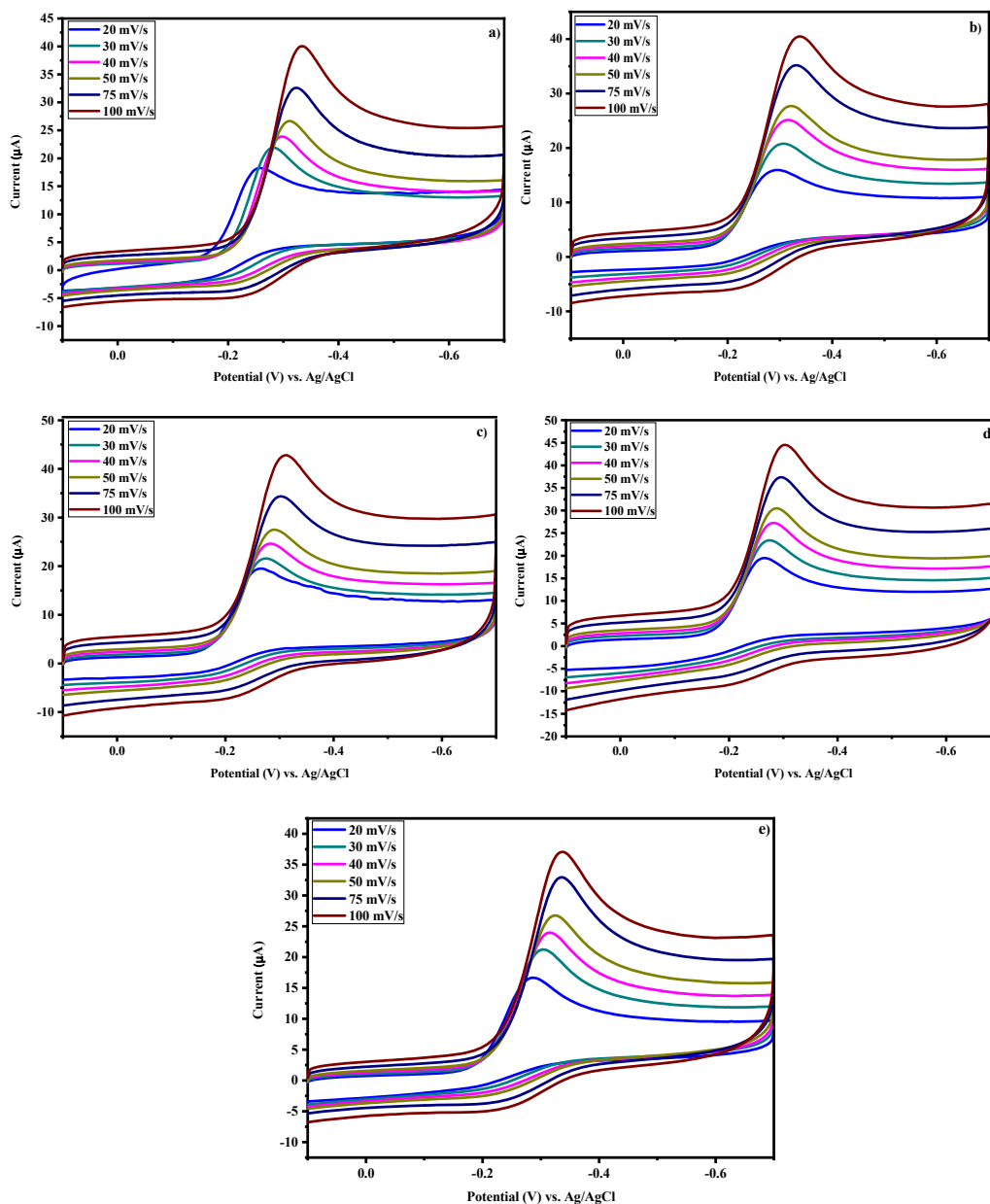
Figure 7. CV curves of (a) MnO₂; (b) Ag–MnO₂-2.5; (c) Ag–MnO₂-5; (d) Ag–MnO₂-7.5; (e) and Ag–MnO₂-10; modified electrodes at various scan rate (20–100 mV/s) in aqueous 0.1 M KOH.

Moreover, for bare GCE and MnO₂ electrode, the onset potential for oxygen reduction is -0.28 V and -0.25 V vs. Ag/AgCl correspondingly. After doped with Ag both the cathodic reduction peak potential and onset potential of Ag–MnO₂-7.5/GCE have been significantly positively shifted to −0.29 V and −0.17 V correspondingly, at a scan rate of 50 mV/s demonstrating the improvement of ORR activity. Finally, compared with bare GCE, and Ag–MnO₂-7.5 (Ag–MnO₂/GCE), the peak current of 23.22 μA (GCE) was increased 30.45 μA (Ag–MnO₂/GCE) and the peak potential was shifted from −0.35 V to −0.285 V at a scan rate of 50 mV/s (Figure 6d).

The results presented that the Ag–MnO₂-7.5 nanoparticles show a high catalytic activity for the reduction of O₂ [39]. These results display that the catalytic performance of Ag doped MnO₂ has been highly improved by the synergistic effect of Ag and MnO₂ nanoparticles [40]. It is supposed that the improvement of oxygen reduction performance is because of lattice activation and oxygen defects by Ag doping [41].

Moreover, Figure 7 displays the CV result of MnO₂, Ag–MnO₂-2.5, Ag–MnO₂-5, Ag–MnO₂-7.5, and Ag–MnO₂-10 modified electrodes

saturated in O₂-saturated at various scan rates (20–100 mV/s). Hence, using a potential window of 0.1–0.7 V, the CV curves of all the working electrodes were measured from 20 to 100 mV s⁻¹. The remarkable stability of the working electrode in aqueous electrolyte, without any

Table 2. Cₛ results of MnO₂ and Ag–MnO₂ modified electrodes computed from CV results at different scan rates.

Scan rate (mV/s)	Specific capacitance (F/g)				
	MnO₂	Ag–MnO₂-2.5	Ag–MnO₂-5	Ag–MnO₂-7.5	Ag–MnO₂-10
20	150.9	180.7	210.9	250.1	150.4
30	160.8	200.5	230.2	260.8	160.6
40	180.9	220.6	250.4	290.6	190.1
50	200.5	240.5	270.0	310.7	200.7
75	230.4	250.9	290.5	340.9	230.2
100	330.0	290.0	370.3	390.1	270.2

Table 3. Comparison of C_s values of MnO$_2$-based electrodes recently reported in the literature.

Electrode material	Methods[a]	Current density/ Scan rate	Electrolyte Type & Concentration	Capacitance (F g^{-1})	Ref.
Graphene/ amorphous α-MnO$_2$ composite	CD	1 A.g^{-1}	1 M KOH	367	[44]
Branched α-MnO$_2$ nanorods	CD	2 A.g^{-1}	1.0 M Na$_2$SO$_4$	182	[45]
MnO$_2$@MnO$_2$	CD	0.5 A.g^{-1}	6.0 M KOH	310	[46]
MnO$_2$/ graphene hybrid	CV	200 mV/s	1.5 M Li$_2$SO$_4$	326.33	[47]
Fiber-like MnO$_2$	CV	10 mV/s	0.5 M Na$_2$SO$_4$	92	[48]
Ag–MnO$_2$	CV	100 mV/s	6.0 M KOH	390.1	This work

breakdown, is indicated by the CV curves' continued rise in linearity with an increase in scan rate. Additionally, the efficient ion diffusion at the electrode/electrolyte interface during the CV measurement was revealed by the linearity of the growing ratio of the specific capacitance with the growth of the CV curves. The CV curve for MnO$_2$ and Ag–MnO$_2$ NPs at different concentration of Ag is presented in Figure 7(a, b, c, d, e), demonstrating that the reduction peak potential were shifted towards the

lower energy side with increasing dopant concentration. The reduction peak potential shift towards the negative side implies the irreversible reaction [42].

The Cs values of all electrodes at various scan rates are showed in Table 2. Hence, Ag–MnO$_2$-7.5 is displaying the highest capacitive values (390.1 F g^{-1}) as associated to other electrodes at 100 mV/s scan rate. The result shows higher capacitive value associated to the reported capacitive results of MnO$_2$-based electrodes [43]. Table 3 shows the comparison of capacitive values of MnO$_2$-based electrodes reported in literature.

3.6.2. CV scanning rate analysis

The scanning rate effect of Ag/α-MnO$_2$/GCE on ORR was investigated using CV as presented in Figure 8a. The reduction peak current of as-prepared nanomaterials was increases as the increase of scanning rate as well as potential shift to the negative direction was observed [49]. Hence, in the range of 20–100 mV/s there is a linear relationship among square root of scanning rate ($v^{1/2}$) and reduction peak currents, which showed that the electrochemical characteristics of ORR at the Ag/α-MnO$_2$/GCE modified electrode is a diffusion-controlled process and the corresponding equation (Eq. (5)) can be expressed as follows (Figure 8b) [50]:

$$I_{pc}(\mu A) = 5.2228 \ v^{1/2}(V^{1/2}s^{-1/2}) - 0.8746, (R^2 = 0.98025) \quad (5)$$

Figure 8c shows the linear relationship of peak current with v which suggests the presence of electroactive species adsorption. The findings confirm that the ORR on the Ag/α-MnO$_2$/GCE is a mixture of kinetic control and diffusion reactions, including the adsorption of O$_2$ molecules
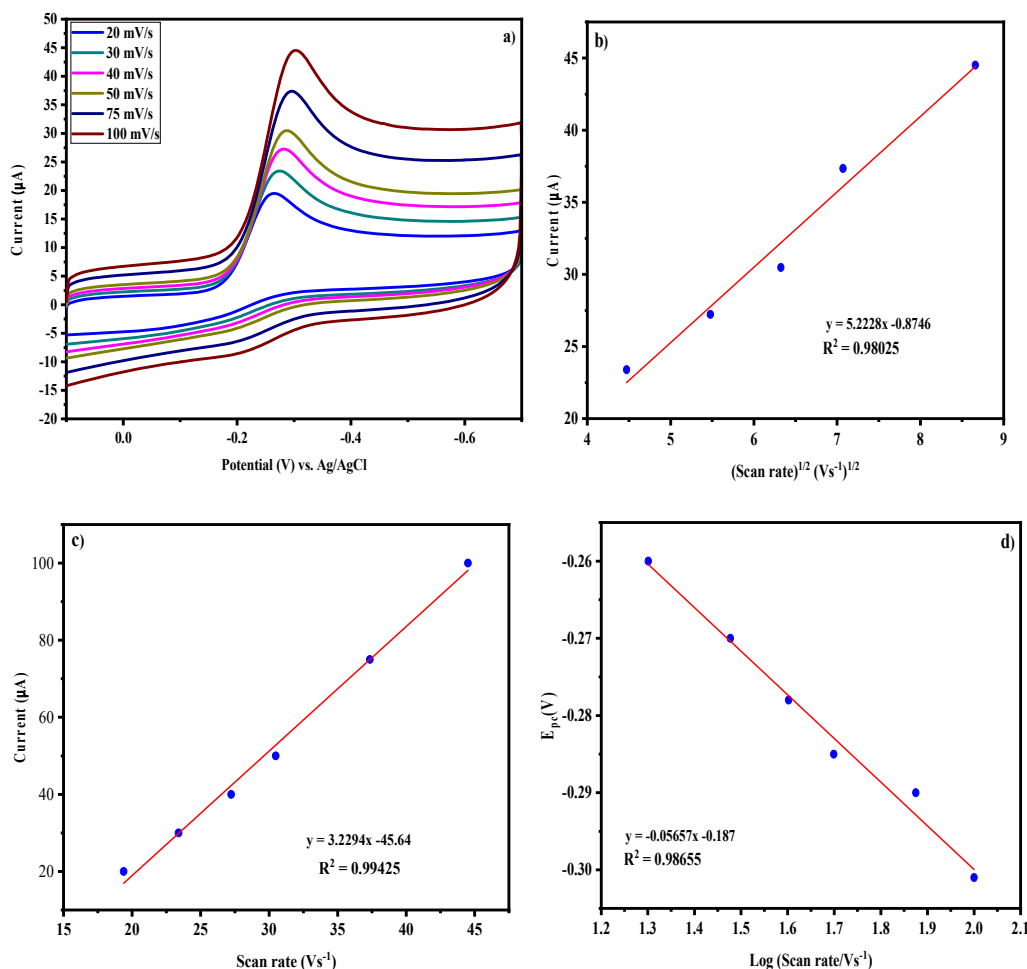

Figure 8. (a) CVs of Ag/α-MnO$_2$/GCE at different scan rates (20–100 mV/s) in 0.1 KOH purged solution. (b) Plot of the cathodic peak current vs. $v^{1/2}$. (c) Plot of the cathodic peak current vs. v. (d) Plot of E$_{pc}$ vs. log (v).
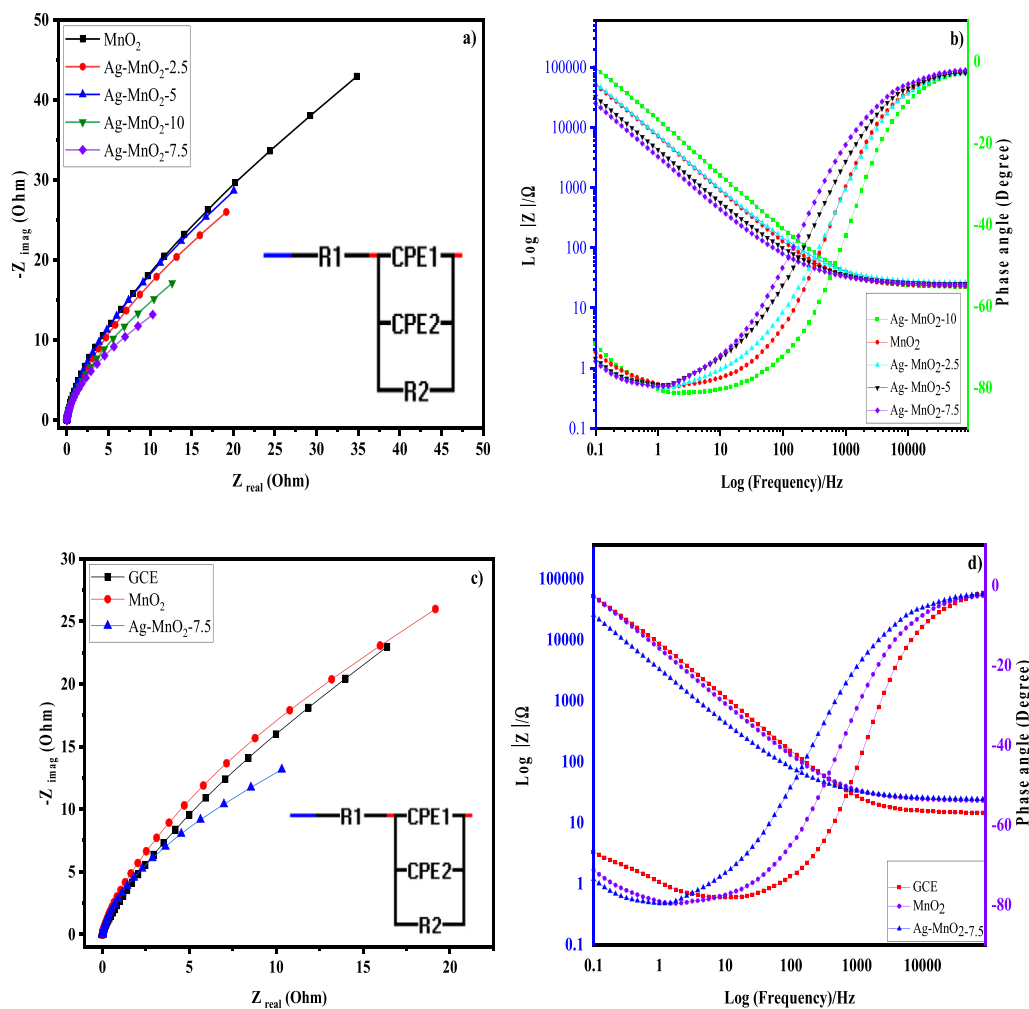
Figure 9. (a) Nyquist results and the corresponding equivalent circuit of MnO_2, Ag–MnO_2-2.5, Ag–MnO_2-5, Ag–MnO_2-7.5 and Ag–MnO_2-10. (b) Bode plots of MnO_2, Ag–MnO_2-2.5, Ag–MnO_2-5, Ag–MnO_2-7.5 and Ag–MnO_2-10. (c) Nyquist results of GCE (bar), MnO_2, Ag–MnO_2-7.5. (d) Bode plots of GCE (bar), MnO_2, Ag–MnO_2-7.5.

on the electrode surface [51]. Figure 8d shows the linear relationship between v vs logarithmic sweep rate as expressed in Eq. (6).

$$E_{pc}(V) = 3.2294 \log v(Vs^{-1}) - 44.64, (R^2 = 0.9942) \qquad (6)$$

Moreover, for an irreversible CV behaviour, the number of electrons (n) involved in the reduction of O_2 at Ag/α-MnO_2/GCE was determined by Laviron equation (Eq. (7) [52].

$$E_{pc} = E^{0'} + \left(\frac{2.303\,RT}{\alpha nF}\right)\log\left(\frac{RT\,k^0}{\alpha nF}\right)\left(\frac{2.303\,RT}{\alpha nF}\right)\log v \qquad (7)$$
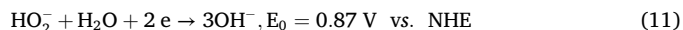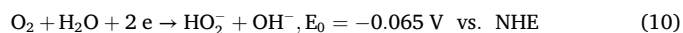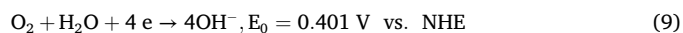
where E_{pc}, $E^{0'}$, F, T, k°, R and α were cathodic peak potential, redox potential, Faraday constant, temperature in Kelvin, standard heterogeneous rate constant of the reaction, gas constant, and the transfer coefficient, correspondingly.

Thus, the value of αn can be simply computed from the slope of E_p vs. log v. In this plot, the slope is 0.056, taking 298 K, 8.314 J/K mol, and 96480 C/mol as T, R and an F value, respectively the result of αn was estimated to be 1.05. Moreover, the value of α can be calculated using Eq. (8) [53];

$$\alpha = \frac{47.7}{E_P - E_{\frac{P}{2}}}\,mV \qquad (8)$$

where $E_{p/2}$ and E_p are half-wave potential and the peak potential, respectively. Hence, from Eq. (8) we calculated the value of α to be 0.27.

Therefore, the transferred number of electrons (n) in the reduction of O_2 of at Ag/α-MnO_2/GCE was computed to be 3.89. The obtained result showed that n is close to 4 which indicate that without the formation H_2O_2 as an intermediate product dissolved O_2 is directly reduced to H_2O [54]. The ORR mechanism of the as-prepared catalysts can be takes place either through the direct 4e⁻ process (Eq. (9)) or the 2e⁻ process (Eq. (10)). For the latter, peroxide ions are first produced followed by the reduction (Eq. (11)) of the peroxide.

$$O_2 + H_2O + 4\,e \rightarrow 4OH^-, E_0 = 0.401\ V\ \ vs.\ \ NHE \qquad (9)$$

$$O_2 + H_2O + 2\,e \rightarrow HO_2^- + OH^-, E_0 = -0.065\ V\ \ vs.\ \ NHE \qquad (10)$$

$$HO_2^- + H_2O + 2\,e \rightarrow 3OH^-, E_0 = 0.87\ V\ \ vs.\ \ NHE \qquad (11)$$

The 4e⁻ ORR is appropriate for ZABs utilization, and the generation of peroxide throughout the ORR needs to be reduced as it can chemically attack catalyst support and catalysts. The following theory was used to compute the ORR at the Ag or Mn site. According to most reports, the four-electron mechanism that causes the ORR under base conditions follows these steps (Eqs. (12), (13), (14), (15), and (16)) [55]:

$$O_2(g)\ +\ ^* \Rightarrow O_2^* \qquad (12)$$

$$O_2^* + H_2O(l) + e^- \Rightarrow OOH^* + OH^- \qquad (13)$$

Table 4. EIS parameters recorded via fitting data of an equivalent circuit model.

Parameters	GCE	MnO$_2$	Ag–MnO$_2$-2.5	Ag–MnO$_2$-5	Ag–MnO$_2$-7.5	Ag–MnO$_2$-10
R1(Ω)	28.835	24.268	28.045	26.735	23.586	26.304
R2(Ω)	1.2 × 06	6.24 × 05	8.04 × 05	4.93 × 05	3.59 × 05	1 × 06
CPE1-T [sP/Ω]	1.9E − 05	2.4E − 05	2.1E − 05	3.6E − 05	4.9E − 05	8.4E − 07
P	0.89	0.87	0.86	0.85	0.86	0.41
CPE2-T [sP/Ω]	7.6E − 06	5.4E − 06	6.6E − 06	1.2E − 05	1.1E − 05	1.5E − 05
P	0.89	0.87	0.86	0.85	0.86	0.89

$$OOH* + e^- \Rightarrow O* + OH^- \tag{14}$$

$$O* + H_2O(l) + e^- \Rightarrow OH* + OH^- \tag{15}$$

$$OH* + e^- \Rightarrow OH^- + * \tag{16}$$

where * refers to a surface's active site that corresponds to the given one.

3.6.3. Electrochemical impedance spectroscopy (EIS) study

EIS is a powerful method to investigate the capacitance, internal resistance and basic characteristics of electrode materials in the electrolyte. The EIS analyses were accomplished at room temperature to gain information on the electrode materials charge-transfer resistance, phase angle, interface and surface [56]. The impedance data are examined using a Nyquist and bode plot, which displays the frequency profile of the as-prepared electrode. Nyquist plots are represented on the X-axis with
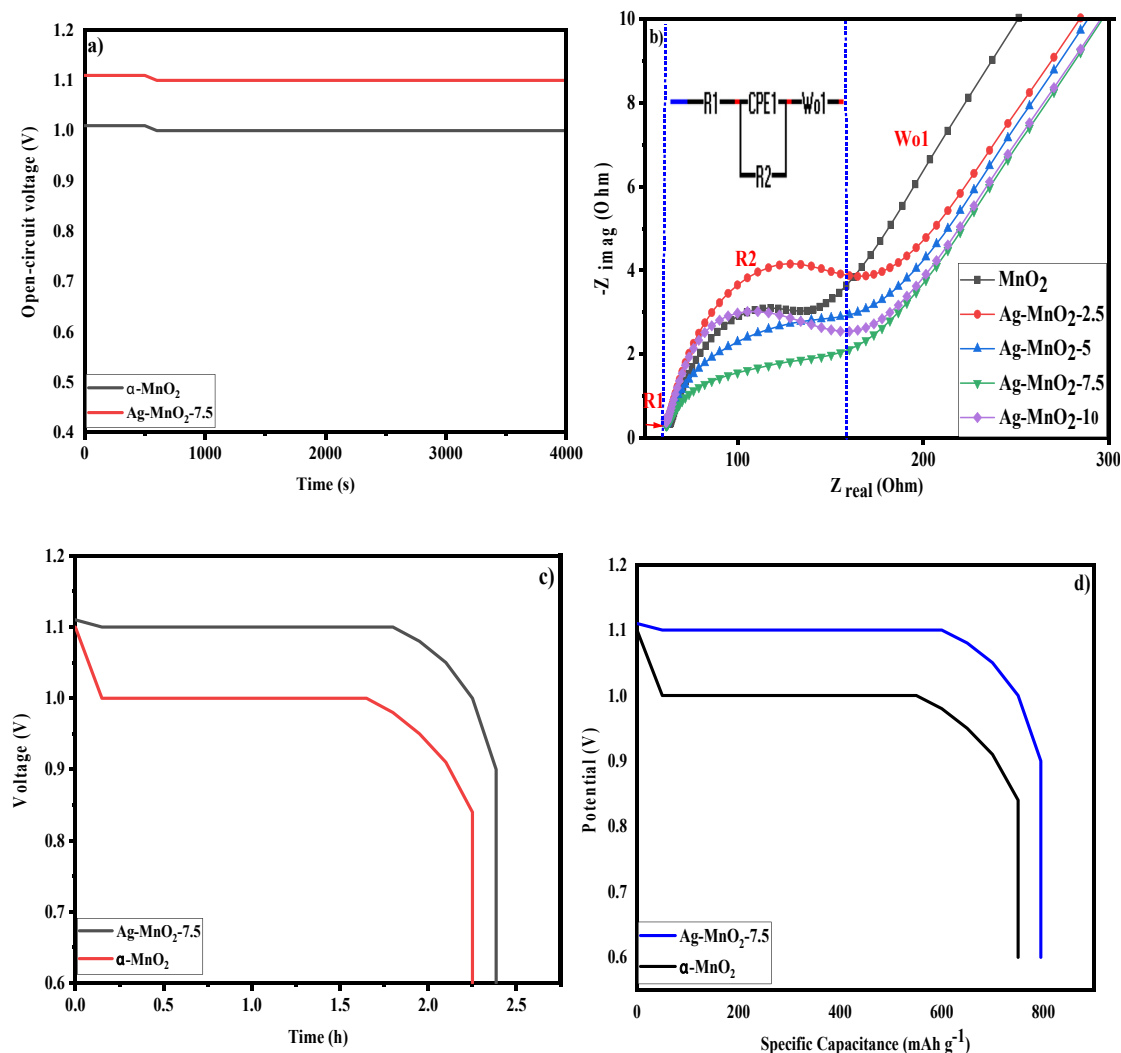

Figure 10. (a) Open-circuit potentials of assembled ZABs through α-MnO$_2$, Ag-α-MnO$_2$-2.5, Ag-α-MnO$_2$-5, Ag-α-MnO$_2$-7.5 and Ag-α-MnO$_2$-10 electrodes. (b) Nyquist profile of the assembled ZABs through α-MnO$_2$, Ag-α-MnO$_2$-2.5, Ag-α-MnO$_2$-5, Ag-α-MnO$_2$-7.5 and Ag-α-MnO$_2$-10 electrodes; inset shows the Equivalent circuit ZABs using α-MnO$_2$, Ag-α-MnO$_2$-2.5, Ag-α-MnO$_2$-5, Ag-α-MnO$_2$-7.5 and Ag-α-MnO$_2$-10 electrodes. In the equivalent circuit illustration, R1 is the bulk resistance of the cell (electrolyte and electrodes); R2 is the charge transfer resistance, CPE1 is a constant phase element (capacitance of the interfacial layer); Wo1 is the Warburg impedance (ion diffusion in the electrolyte). (c) Discharge profile of ZABs using Ag-α-MnO$_2$-7.5 and α-MnO$_2$ electrodes at a constant current density of 1 mA/cm^2. (d) Specific discharge capacities of zinc-air batteries with α-MnO$_2$ and Ag–MnO$_2$-7.5 air cathodes.

Table 5. EIS fitting results for the fabricated ZABs with different electrodes.

Sample	R1 [Ω]	R2 [Ω]	CPE1	
			T [sP/Ω]	P
MnO₂	61.984	89.238	6.2676E − 05	0.7
Ag–MnO₂-2.5	59.718	125.14	4.7405E − 05	0.71
Ag–MnO₂-5	59.867	92.381	0.00012972	0.63
Ag–MnO₂-7.5	58.068	48.722	9.4393E − 05	0.69
Ag–MnO₂-10	63.836	78.945	2.4432E − 05	0.78

the real part (Z′) and on the Y-axis with the imaginary part (-Z″) in the 0.01 kHz–100 kHz frequency regimes as reported in Figure 9. Moreover, the Nyquist plot a high frequency consists of semicircles associated with the electron transfer limited process. Furthermore, the semicircle diameter presents the electron transfer resistance (R_{ct}), and its lower value matches a faster electron transfer rate [57]. Figure 9a, indicates the Nyquist results of MnO₂, Ag–MnO₂-2.5, Ag–MnO₂-5, Ag–MnO₂-7.5, and Ag–MnO₂-10 modified electrodes and their corresponding equivalent circuits in 6M KOH. Bode plot of phase angle with respect to log (f/Hz) of the MnO₂, Ag–MnO₂-2.5, Ag–MnO₂-5, Ag–MnO₂-7.5 and Ag–MnO₂-10 modified electrodes and GCE in 6 M KOH solution are shown in Figure 9(b) and (d), correspondingly. The phase angles of as-prepared electrodes lie in the range of 50–70° at low frequency (<100 Hz), which implies the ideal capacitive and redox performance of the electrodes [58]. EIS spectrum analyser software was utilized for EIS data fitting as shown in Figure 9. The impedance spectra of as-prepared electrodes Nyquist plots were studied using fitting the experimental data to the same equivalent circuit models that contains of R1, R2, CPE1, and CPE2 which refers as electrolyte resistance, electron transfer resistance, constant phase element of double layer capacitance and constant phase element of the electrode capacitance, correspondingly. Table 4 shows the fitted parameters gained from the EIS data of as prepared electrodes. The parameters n1 and n2 denotes to constant phase for CPE1 and CPE2, correspondingly. If the value of n (n1 and n2) approaches to 1 is the indicator of more capacitive performance. Hence, the highest value of n is 1. Moreover, the connection of CPE in parallel with a resistance shows the occurrence of a non-Faradaic reaction (charge accumulation at the interface) and a faradaic reaction (charge transfer). The interfacial interaction among the electrolyte and the catalyst is directly related to the Rct value [59]. In addition, the parallel connection of CPE1 and R2 largely depends on the dielectric properties at the electrode/electrolyte interface. Hence, parameters (CPE1 and R2) are affected by the electrode surface modification and gave rise to the semicircle property change particularly R2 which depends on the electron transfer at the electrode interface. The measured value of R1 follows the order GCE (28.835 Ω) > Ag–MnO₂-2.5 (28.045 Ω) > Ag–MnO₂-5 (26.735 Ω) > Ag–MnO₂-10 (26.304 Ω) > MnO₂ (24.268Ω) > Ag–MnO₂-7.5 (24.268Ω) while the R2 follows the order GCE (1.2 × 06 Ω) > Ag–MnO₂-10 (1 × 06 Ω) >

Ag–MnO₂-2.5 (8.04 × 05 Ω) > Ag–MnO₂-5 (4.93 × 05Ω) > Ag–MnO₂-7.5 (3.59 × 05 Ω). Moreover, when the CPE exponent *n1* and *n2* remain closer to 1 for the GCE, MnO₂, Ag–MnO₂-2.5, Ag–MnO₂-5, and Ag–MnO₂-7.5 both the Ag–MnO₂-10, showed the values of 0.41 for *n1* confirming high porosity nature of the materials. Hence, Ag–MnO₂-7.5 electrode shows a smaller Rct value which is the indicator of excellent charge transport property [58]. Thus, faster electron transport accelerates the oxygen reduction speed in accordance to the maximum reduction current found from the Ag–MnO₂-7.5 nanoparticles (Figure 6). Moreover, smaller Rct value is vital to decrease the overpotential in ORR for the MnO₂-NTs/graphene composite. The higher charge transport characteristic and better ORR activity of Ag–MnO₂-7.5 nanoparticles are due to the synergetic effect of Ag and MnO₂ NPs [60].

3.6.4. Application in zinc-air battery

The open-circuit potential (OCP) vs. time of MnO₂ and Ag–MnO₂-7.5 based ZABs are presented in Figure 10a [61]. The electrochemical performances of zinc-air batteries cells were further examined through EIS as shown in Figure 10b. The impedance at high frequency region correlated with the charge transfer processes, which might be consisting of the ion and electron transfer routes. Additionally, the low-frequency region of the straight line is attributed to diffusion processes, correspond to the adsorption–desorption of oxygen, the surface diffusion of intermediate oxygen species and oxygen diffusion at the air electrode interface [62]. Indeed, the impedance profiles were fit to an equivalent circuit as presented in Figure 10b [63]. The EIS data equivalent circuit consists of R1, R2, CPE1 and Wo1 which corresponds to bulk resistance of the cell (electrolyte and electrodes), charge-transfer resistor, constant phase element and a Warburg element, respectively. The constant phase element (CPE) is comprised by two components; CPE-T and CPE-P. CPE-T is a pseudo capacitance which is called Q and CPE-P is related to the semi-circle in the Nyquist plot (depressed semicircle), normally used by the notation 'n'. Moreover, the equivalent fitting parameters (R1, R2, CPE1-T and CPE1-P) are reported in Table 5. Both ohmic resistances and electrolyte resistance are significantly reduced after MnO₂ was modified with Ag. The next resistance is ascribed to R2 produced by the charge-transfer resistor [64]. Moreover, the last resistance is attributed to the Warburg resistance (Wo1) shown by the straight line at low frequency region which is associated with the diffusion properties on the interface among the electrolyte and the catalysts surface. Thus, electrolyte resistance and charge-transfer resistance of battery with Ag–MnO₂-2.5, Ag–MnO₂-5 and Ag–MnO₂-7.5 catalysts showed improved intrinsic conductivity due to the introduction of Ag nanoparticles (Table 5). Hence, Ag possesses good catalytic activity for oxygen surface diffusion, dissociation of molecular oxygen into atomic oxygen, best conductivity, and oxygen surface adsorption.

Discharge profile of ZABs with 6 M KOH solution at a constant current density of 1 mA/cm² is presented in Figure 10c. The analysis showed that the Ag doped α-MnO₂ sample took nearly 2.38 h discharge time, which was longer than that of α-MnO₂ (2.25 h), demonstrating that catalytic
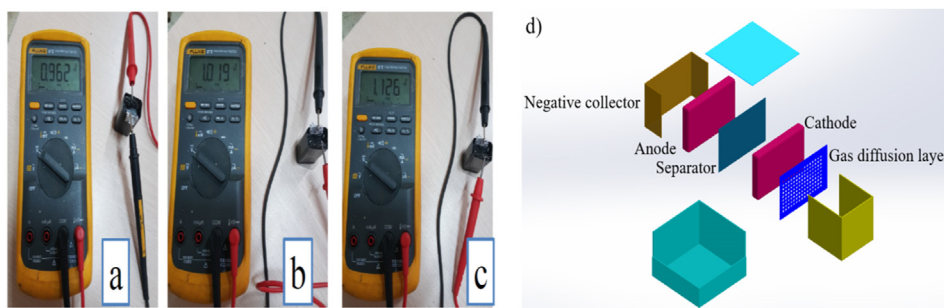

Figure 11. (a–c) Photographic demonstration of the open circuit potential of the homemade ZAB assembled with zinc foil, α-MnO₂ and Ag doped α-MnO₂ cathode and 6 M KOH electrolyte solution and (d) Configuration of rechargeable assembled zinc air battery.

performance of Ag doped α-MnO$_2$-7.5 is improved due to the loading of Ag.

Further, α-MnO$_2$ catalyst based battery delivered a specific capacity of 750 mA h g^{-1} with corresponding energy density ~825 Wh kg^{-1} whereas Ag–MnO$_2$-7.5 based battery showed a specific capacity of 795 mA h g^{-1} with corresponding high energy density ~875 Wh kg^{-1} at 1 mA cm^{-2} discharging conditions (Figure 10d). In Figure 11(a, b, c) the screen of a multimeter displays the open circuit potential of 0.962 V, 1.019 V and 1.1.126 V for α-MnO$_2$, Ag doped α-MnO$_2$- 2.5 and Ag doped α-MnO$_2$- 7.5 electrodes of homemade ZABs, respectively. Thus, a home-made battery with Ag doped α-MnO$_2$ electrocatalyst showed higher open circuit potential than that of α-MnO$_2$. The batteries were assembled using zinc foil, α-MnO$_2$ and Ag doped α-MnO$_2$-based gas diffusion electrode and 6 M KOH electrolyte solution (Figure 11d) [65]. All of the results show that the Ag–MnO$_2$-7.5 has excellent potential as an electrocatalyst in the zinc-air battery.

4. Conclusion

In this study, we have used a facile co-precipitation approach to develop Ag doped MnO$_2$ NPs as a high performance ORR catalyst for ZABs. Herein, the CV profile demonstrated that the ORR activity of Ag doped α-MnO$_2$ NPs are higher than pure α-MnO$_2$. Among the doping concentration of Ag doped α-MnO$_2$ nanoparticles, 7.5 mmol of Ag doped MnO$_2$ presented the best catalyst loading that produced the highest ORR potential and current. The ORR performance of Ag doped MnO$_2$ nanoparticles were significantly increased when it was modified using Ag NPs in alkaline medium, which makes Ag doped MnO$_2$ catalyst one of the best cathode material for ZABs. The Ag doped MnO$_2$ nanoparticles followed a 4-electron pathway in ORR because of the synergistic result among Ag and MnO$_2$ nanoparticles. EIS confirms the loading of Ag NPs improved the conductivity by decreasing the charge transfer resistant of the air electrode. In full cell tests, Ag doped MnO$_2$ showed a lower resistance and higher conductivity than MnO$_2$ NPs when utilized as an air electrode in zinc-air batteries. Moreover, Ag and MnO$_2$ catalysts can be noticed as a best candidate for ZABs due to their low cost and high performance, which replaces the expensive Pt/C electrocatalysts.

Declarations

Author contribution statement

Ababay Ketema Worku: Conceived and designed the experiments; Performed the experiments; Analyzed and interpreted the data; Wrote the paper.

Delele Worku Ayele, Nigus Gabbiye Habtu: Analyzed and interpreted the data; Contributed reagents, materials, analysis tools or data; Wrote the paper.

Mehary Dagnew Ambaw: Conceived and designed the experiments; Wrote the paper.

Data availability statement

Data will be made available on request.

Declaration of interests statement

The authors declare no conflict of interest

Additional information

No additional information is available for this paper.

References

[1] H.R. Barai, A.N. Banerjee, S.W. Joo, Improved electrochemical properties of highly porous amorphous manganese oxide nanoparticles with crystalline edges for superior supercapacitors, J. Ind. Eng. Chem. 56 (2017) 212–224.

[2] Q. Liu, S. Ji, J. Yang, H. Wang, B.G. Pollet, R. Wang, Enhanced cycleability of amorphous MnO2 by covering on α-MnO2 needles in an electrochemical capacitor, Materials 10 (2017).

[3] N.A. Matrose, K. Obikese, Z.A. Belay, O.J. Caleb, Micropores regulating enables advanced carbon sphere catalyst for Zn-air batteries, Sci. Total Environ. (2019), 135907.

[4] X.F. Lu, Y. Chen, S. Wang, S. Gao, X.W. Lou, Interfacing manganese oxide and cobalt in porous graphitic carbon polyhedrons boosts oxygen electrocatalysis for Zn–air batteries, Adv. Mater. 31 (2019), 1902339.

[5] V.M. Tran, A.T. Ha, M.L.P. Le, Capacitance behavior of nanostructured ε-MnO2/C composite electrode using different carbons matrix, Adv. Nat. Sci. Nanosci. Nanotechnol. 5 (2014).

[6] L. Ye, Y. Hong, M. Liao, B. Wang, D. Wei, H. Peng, Recent advances in flexible fiber-shaped metal-air batteries, Energy Storage Mater. 28 (2020) 364–374.

[7] A.K. Worku, D.W. Ayele, N.G. Habtu, Recent advances and future perspectives in engineering of bifunctional electrocatalysts for rechargeable zinc–air batteries, Mater. Today Adv. 9 (2021), 100116.

[8] B. Huang, X. Zhang, J. Cai, W. Liu, S. Lin, A novel MnO2/rGO composite prepared by electrodeposition as a non-noble metal electrocatalyst for ORR, J. Appl. Electrochem. 49 (2019) 767–777.

[9] F. Golmohammadi, M. Amiri, Fabrication of MEA from biomass-based carbon nanofibers composited with nickel-cobalt oxides as a new electrocatalyst for oxygen reduction reaction in passive direct methanol fuel cells, Electrocatalysis 11 (2021) 485–496.

[10] A.K. Worku, D.W. Ayele, N.G. Habtu, T.A. Yemata, Engineering Co3O4/MnO2 nanocomposite materials for oxygen reduction electrocatalysis, Heliyon 7 (2021), e08076.

[11] K. Liu, X. Huang, H. Wang, F. Li, Y. Tang, J. Li, M. Shao, Co3O4-CeO2/C as a highly active electrocatalyst for oxygen reduction reaction in Al-air batteries, ACS Appl. Mater. Interfaces 8 (2016) 34422–34430.

[12] H. Ma, B. Wang, Y. Fan, W. Hong, Development and characterization of an electrically rechargeable zinc-air battery stack, Energies 7 (2014) 6549–6557.

[13] A.K. Worku, D.W. Ayele, N.G. Habtu, B.T. Admasu, G. Alemayehu, B.Z. Taye, T.A. Yemata, Energy storage technologies; recent advances, challenges, and prospectives, in: A.K. Bohre, P. Chaturvedi, M.L. Kolhe, S.N. Singh (Eds.), Plan. Hybrid Renew. Energy Syst. Electr. Veh. Microgrid Model. Control Optim., Springer Nature Singapore, 2022, pp. 125–150.

[14] S. Ramesh, K. Karuppasamy, H.S. Kim, H.S. Kim, J.H. Kim, Hierarchical Flowerlike 3D nanostructure of Co3O4@MnO2/N-doped Graphene oxide (NGO) hybrid composite for a high-performance supercapacitor, Sci. Rep. 8 (2018) 1–12.

[15] J. Fu, J. Zhang, X. Song, H. Zarrin, X. Tian, J. Qiao, L. Rasen, K. Li, Z. Chen, A flexible solid-state electrolyte for wide-scale integration of rechargeable zinc-air batteries, Energy Environ. Sci. 9 (2016) 663–670.

[16] C.W. Woon, M.A. Islam, B. Ethiraj, H.R. Ong, C.K. Cheng, K.F. Chong, G. Hedge, M.M.R. Khan, Carbon nanotube-modified MnO2: an efficient electrocatalyst for oxygen reduction reaction, ChemistrySelect 2 (2017) 7637–7644.

[17] Q. Liu, Z. Pan, E. Wang, L. An, G. Sun, Aqueous metal-air batteries: fundamentals and applications, Energy Storage Mater. 27 (2020) 478–505.

[18] V. Veeramani, B. Dinesh, S.M. Chen, R. Saraswathi, Electrochemical synthesis of Au-MnO2 on electrophoretically prepared graphene nanocomposite for high performance supercapacitor and biosensor applications, J. Mater. Chem. A. 4 (2016) 3304–3315.

[19] J. Zhang, D. Rao, J. Zheng, Synthesis of Ag nanoparticle doped MnO2/GO nanocomposites at a gas/liquid interface and its application in H2O2 detection, Electroanalysis 28 (2016) 588–595.

[20] S. Khamsanga, R. Pornprasertsuk, T. Yonezawa, A.A. Mohamad, S. Kheawhom, δ-MnO2 nanoflower/graphite cathode for rechargeable aqueous zinc ion batteries, Sci. Rep. 9 (2019) 1–10.

[21] A.K. Worku, D.W. Ayele, N.G. Habtu, M.A. Teshager, Z.G. Workineh, Recent progress in MnO2-based oxygen electrocatalysts for rechargeable zinc-air batteries, Mater. Today Sustain. (2021), 100072.

[22] J. Qian, J. Li, J. Bxia, J. Zhang, Z. Zhang, C. Guan, D. Gao, W. Huang, Multi-stability modulating of alkaline-earth metal doped LaCoO3 for rechargeable Zn-air batteries, Energy Storage Mater. 42 (2021) 470–476.

[23] T.N.T. Pham, Y.S. Yoon, Development of nanosized Mn3O4-Co3O4 on multiwalled carbon nanotubes for cathode catalyst in urea fuel cell, Energies 13 (2020) 1–13.

[24] H. Song, H. Zhao, X. Zhang, Y. Xu, X. Cheng, S. Gao, L. Huo, A hollow urchin-like α-MnO 2 as an electrochemical sensor for hydrogen peroxide and dopamine with high selectivity and sensitivity, Microchim. Acta 186 (2019).

[25] A. Girimonte, A. Stefani, M. Innocenti, C. Fontanesi, R. Giovanardi, Influence of magnetic field on the electrodeposition and capacitive performances of mno2, Magnetochemistry 7 (2021) 1–18.

[26] A.K. Worku, D.W. Ayele, N.G. Habtu, Influence of nickel doping on MnO2 nanoflowers as electrocatalyst for oxygen reduction reaction, SN Appl. Sci. 3 (2021).

[27] L. Song, Y. Duan, J. Liu, H. Pang, Lattice mismatch for broadband microwave absorption, Compos. Part B. 199 (2020), 108318.

[28] Y. Zhou, P. Jin, Y. Zhou, Y. Zhu, High-performance symmetric supercapacitors based on carbon nanotube/graphite nanofiber nanocomposites, Sci. Rep. 8 (2018) 1–7.

[29] S. Nagamuthu, S. Vijayakumar, G. Muralidharan, Biopolymer-assisted synthesis of λ-MnO2 Nanoparticles as an electrode material for aqueous symmetric supercapacitor devices, Ind. Eng. Chem. Res. 52 (2013) 18262–18268.

[30] S. Khilari, S. Pandit, M.M. Ghangrekar, D. Das, D. Pradhan, Graphene supported α-MnO2 nanotubes as a cathode catalyst for improved power generation and wastewater treatment in single-chambered microbial fuel cells, RSC Adv. 3 (2013) 7902–7911.

[31] H. Ma, B. Wang, A bifunctional electrocatalyst α-MnO2-LaNiO3/carbon nanotube composite for rechargeable zinc-air batteries, RSC Adv. 4 (2014) 46084–46092.

[32] F.W.T. Goh, Z. Liu, X. Ge, Y. Zong, G. Du, T.S.A. Hor, Ag nanoparticle-modified MnO2 nanorods catalyst for use as an air electrode in zinc–air battery, Electrochim. Acta 114 (2013) 598–604.

[33] R. Poonguzhali, N. Shanmugam, R. Gobi, A. Senthilkumar, G. Viruthagiri, N. Kannadasan, Effect of Fe doping on the electrochemical capacitor behavior of MnO2 nanocrystals, J. Power Sources 293 (2015) 790–798.

[34] E. Hastuti, A. Subhan, P. Amonpattaratkit, M. Zainuri, S. Suasmoro, The effects of Fe-doping on MnO2: phase transitions, defect structures and its influence on electrical properties, RSC Adv. 11 (2021) 7808–7823.

[35] I. Sultana, M. Idrees, M. Yasir Rafique, S. Ilyas, S.Q. Hussain, A.A. Kahn, A. Razaq, Electrodeposition of silver (Ag) nanoparticles on MnO2 nanorods for fabrication of highly conductive and flexible paper electrodes for energy storage application, J. Mater. Sci. Mater. Electron. 29 (2018) 20588–20594.

[36] S.A. Alzahrani, S.A. Al-Thabaiti, W.S. Al-Arjan, M.A. Malik, Z. Khan, Preparation of ultra long α-MnO2 and Ag@MnO2 nanoparticles by seedless approach and their photocatalytic performance, J. Mol. Struct. 1137 (2017) 495–505.

[37] G. Li, M.A. Mezaal, K. Zhang, L. Lei, Synthesis and electrocatalytic performance of NiO modified Co3O4 composites for zinc-air batteries, Int. J. Electrochem. Sci. 10 (2015) 5395–5404.

[38] A.L. Bhatti, U. Aftab, A. Tahira, M.I. Abro, M. Kashif Samoon, M.H. Aghem, M.A. Bhatti, Z. Hussainibupoto, Facile doping of nickel into Co3O4 nanostructures to make them efficient for catalyzing the oxygen evolution reaction, RSC Adv. 10 (2020) 12962–12969.

[39] S.A. Pawar, D.S. Patil, J.C. Shin, Transition of hexagonal to square sheets of Co3O4 in a triple heterostructure of Co3O4/MnO2/GO for high performance supercapacitor electrode, Curr. Appl. Phys. 19 (2019) 794–803.

[40] K. Chen, W. Pan, D. Xue, Phase transformation of Ce3+-Doped MnO2 for pseudocapacitive electrode materials, J. Phys. Chem. C 120 (2016).

[41] C. Shi, G.L. Zang, Z. Zhang, G.P. Sheng, Y.X. Huang, G.X. Zhao, X.K. Wang, H.Q. Yu, Synthesis of layered mno2 nanosheets for enhanced oxygen reduction reaction catalytic activity, Electrochim. Acta 132 (2014) 239–243.

[42] M. Lübke, A. Sumboja, L. McCafferty, C.F. Armer, A.D. Handoko, Y. Du, K. McColl, F. Cora, D. Brett, Z. Liu, J.A. Darr, Transition-metal-doped α-MnO2 nanorods as bifunctional catalysts for efficient oxygen reduction and evolution reactions, ChemistrySelect 3 (2018) 2613–2622.

[43] N. Tang, X. Tian, C. Yang, Z. Pi, Q. Han, Facile synthesis of α-MnO2 nanorods for high-performance alkaline batteries, J. Phys. Chem. Solid. 71 (2010) 258–262.

[44] M. Pang, G. Long, S. Jiang, Y. Ji, W. Han, B. Wang, X. Liu, Y. Xi, Rapid synthesis of graphene/amorphous α-MnO2 composite with enhanced electrochemical performance for electrochemical capacitor, Mater. Sci. Eng. B Solid-State Mater. Adv. Technol. 194 (2015) 41–47.

[45] X. Su, X. Yang, L. Yu, G. Cheng, H. Zhang, T. Lin, F.H. Zhao, A facile one-pot hydrothermal synthesis of branched α-MnO2 nanorods for supercapacitor application, CrystEngComm 17 (2015) 5970–5977.

[46] Z. Ma, G. Shao, Y. Fan, G. Wang, J. Song, D. Shen, Construction of hierarchical α-MnO2 Nanowires@Ultrathin δ-MnO2 nanosheets core-shell nanostructure with excellent cycling stability for high-power asymmetric supercapacitor electrodes, ACS Appl. Mater. Interfaces 8 (2016) 9050–9058.

[47] C. Xiong, T. Li, M. Khan, H. Li, T. Zhao, A three-dimensional MnO2/graphene hybrid as a binder-free supercapacitor electrode, RSC Adv. 5 (2015) 85613–85619.

[48] J.Y. Choi, S.J. Park, Effect of manganese dioxide on supercapacitive behaviors of petroleum pitch-based carbons, J. Ind. Eng. Chem. 29 (2015) 408–413.

[49] B.B. Carvalho, V.C.B. Pegoretti, V.G. Celante, P.V.M. Dixini, P.L. Gastelois, W.A.A. Macedo, M.B.J.G. Freitas, Effect of temperature on the electrochemical synthesis of MnO2 recycled from spent Zn–MnO2 alkaline batteries and application of recycled MnO2 as electrochemical pseudocapacitors, Mater. Chem. Phys. 196 (2017) 126–136.

[50] A.K. Worku, D.W. Ayele, N.G. Habtu, M.A. Teshager, Z.G. Workineh, Enhancing oxygen reduction reaction activity of ε-MnO2 nanoparticles via iron doping, J. Phys. Chem. Solid. 157 (2021), 110207.

[51] H.H. Hamzah, N.N. Ahmad Kamal, M. Meneghello, S.A. Shafiee, T. Sönmez, M.N.A. Mohamad Taib, S.H. Mohd Samsuri, M.F. Meor Zulkifli, Hexanediamine monolayer electrografted at glassy carbon electrodes enhances oxygen reduction reaction in aqueous neutral media, J. Electrochem. Soc. 167 (2020) 166508.

[52] E. Laviron, General expression of the linear potential sweep voltammogram in the case of diffusionless electrochemical systems, J. Electroanal. Chem. 101 (1979) 19–28.

[53] A.J.B. Larry, L.R. Faulkner, Electrochemical Methods: Fundamentals and Applications, second ed., Wiley, 2004.

[54] J.I. Gowda, S.T. Nandibewoor, Electrochemical behavior of paclitaxel and its determination at glassy carbon electrode, Asian J. Pharm. Sci. 9 (2014) 42–49.

[55] G. Yang, J. Zhu, P. Yuan, Y. Hu, G. Qu, B.A. Lu, X. Xue, H. Yin, W. Cheng, J. Cheng, W. Xu, J. Li, J. Hu, S. Mu, J.N. Zhang, Regulating Fe-spin state by atomically dispersed Mn-N in Fe-N-C catalysts with high oxygen reduction activity, Nat. Commun. 12 (2021) 4–13.

[56] H. Xia, D. Zhu, Z. Luo, Y. Yu, X. Shi, G. Yuan, J. Xie, Hierarchically structured Co3O4@Pt@MnO2 nanowire arrays for high-performance supercapacitors, Sci. Rep. 3 (2013) 1–8.

[57] A.T. Ezhil Vilian, R. Madhu, S.M. Chen, V. Veeramani, M. Sivakumar, Y.S. Huh, Y.K. Han, Facile synthesis of MnO2/carbon nanotubes decorated with a nanocomposite of Pt nanoparticles as a new platform for the electrochemical detection of catechin in red wine and green tea samples, J. Mater. Chem. B. 3 (2015) 6285–6292.

[58] J.C.M. Costa, M.C. Nascimento, E.C. Silva, B.L. Pereira, R.R. Passos, L.A. Pocrifka, Galvanostatic synthesis of MnO2 in carbon cloth: an electrochemical impedance spectroscopy study, J. Solid State Electrochem. 24 (2020) 1727–1733.

[59] Q. Wu, M. Jiang, X. Zhang, J. Cai, S. Lin, A novel octahedral MnO/RGO composite prepared by thermal decomposition as a noble-metal free electrocatalyst for ORR, J. Mater. Sci. 52 (2017) 6656–6669.

[60] A.K. Worku, D.W. Ayele, N.G. Habtu, M.A. Teshager, Z.G. Workineh, Enhancing oxygen reduction reaction activity of ε-MnO2 nanoparticles via iron doping, J. Phys. Chem. Solid. 157 (2021).

[61] G. Li, M.A. Mezaal, R. Zhang, K. Zhang, L. Lei, Electrochemical performance of MnO2-based air cathodes for zinc-air batteries, Fuel Cell. 16 (2016) 395–400.

[62] M. Ates, O. Kuzgun, Modified carbon black, CB/MnO2 and CB/MnO2/PPy nanocomposites synthesised by microwave-assisted method for energy storage devices with high electrochemical performances, Plast., Rubber Compos. 49 (2020) 342–356.

[63] C. Douard, L. Athouël, D. Brown, O. Crosnier, G. Rebmann, O. Schilling, T. Brousse, Electrode design for mno2-based aqueous electrochemical capacitors: influence of porosity and mass loading, Materials 14 (2021) 1–19.

[64] N. Radenahmad, R. Khezri, A.A. Mohamad, M.T. Nguyen, T. Yonezawa, A. Somwangthanaroj, S. Kheawhom, A durable rechargeable zinc-air battery via self-supported MnOx-S air electrode, J. Alloys Compd. 883 (2021).

[65] A. Chowdhury, K.C. Lee, M.S.W. Lim, K.L. Pan, J.N. Chen, S. Chong, C.M. Huang, G.T. Pan, T.C.K. Yang, The zinc-air battery performance with ni-doped mno2 electrodes, Processes 9 (2021).